

Requirements of Scintillation Crystals with the Development of PET Scanners

Xin Yu ¹, Xi Zhang ¹ , Heng Zhang ¹, Hao Peng ², Qiushi Ren ^{3,4,5,6}, Jianfeng Xu ^{1,*}, Qiyu Peng ^{3,*} and Siwei Xie ^{3,*}

¹ School of Mechanical Science and Engineering, Huazhong University of Science and Technology, 1037 Luoyu Road, Wuhan 430074, China

² School of Physics and Technology, Wuhan University, 299 Bayi Road, Wuhan 430074, China

³ Institute of Biomedical Engineering, Shenzhen Bay Laboratory, Shenzhen 518107, China

⁴ Department of Biomedical Engineering, College of Future Technology, Peking University, Beijing 100871, China

⁵ Peking University Shenzhen Graduate School, Shenzhen 518055, China

⁶ Shenzhen Alpha Laboratory Technology Ltd., Shenzhen 518052, China

* Correspondence: jfxu@hust.edu.cn (J.X.); universalring@163.com (Q.P.); xiesw@szbl.ac.cn (S.X.)

Abstract: Positron emission tomography (PET) is widely used in the diagnosis of tumors, cardiovascular system diseases, and neurological diseases. Scintillation crystals are an important part of PET scanners; they can convert γ photons into fluorescent photons to obtain their energy, time, and position information. Currently, an important research goal in PET is to find scintillation crystals with better performance. In this work, the principle of scintillation crystals is introduced, and the properties and requirements of scintillation crystals in different PET scanners are analyzed. At present, $\text{Lu}_{2(1-x)}\text{Y}_{2x}\text{SiO}_5$ (LYSO) is the scintillation crystal with the best comprehensive properties. LaBr_3 performs even better regarding the timing characteristics and light output; however, LaBr_3 has not been used in any PET scanner because of its deliquescence. Detectors made of $\text{Gd}_3(\text{Ga}, \text{Al})_5\text{O}_{12}$ (GAGG) exhibit a high depth of interaction (DOI) resolution and have considerable application potential. The application fields of PET are constantly expanding, and its future development aims to achieve high spatial resolution and high sensitivity, which require scintillation crystals with better performance.

Keywords: scintillation crystal; positron emission tomography



Citation: Yu, X.; Zhang, X.; Zhang, H.; Peng, H.; Ren, Q.; Xu, J.; Peng, Q.; Xie, S. Requirements of Scintillation Crystals with the Development of PET Scanners. *Crystals* **2022**, *12*, 1302. <https://doi.org/10.3390/cryst12091302>

Academic Editors: Dongsheng Yuan and Riccardo Cerulli

Received: 22 July 2022

Accepted: 2 September 2022

Published: 15 September 2022

Publisher's Note: MDPI stays neutral with regard to jurisdictional claims in published maps and institutional affiliations.



Copyright: © 2022 by the authors. Licensee MDPI, Basel, Switzerland. This article is an open access article distributed under the terms and conditions of the Creative Commons Attribution (CC BY) license (<https://creativecommons.org/licenses/by/4.0/>).

1. Overview

Scintillation materials are only slightly affected by temperature and exhibit stable performance; they thus have a wide range of applications in the field of radiation detection [1,2]. There exist many types of scintillation materials. Compared with organic scintillators, scintillation ceramics, and other scintillation materials, inorganic scintillation crystals have the advantages of a high density, a strong stability, a high transparency, and an excellent luminous performance; they have thus become the mainstream choice of scintillation materials [3]. The scintillation phenomenon was first discovered in pure water in 1903 [4], and Rutherford used a ZnS screen to observe α -particle scattering in 1908 [5]. This experiment represents the first time that scintillation crystals have been used to observe the internal structure of atoms, which is considered to be the starting point of modern physics. NaI (Tl), which was discovered in 1948, is the first scintillation crystal to exhibit excellent scintillation performance [6,7].

In the same period, the invention of photomultiplier tubes (PMTs) enabled weak light signals produced by scintillation crystals to be accurately detected [8], and detectors made of scintillation crystals and photosensors could accurately measure high-energy γ photons. Since then, many types of scintillation crystals have been discovered, and various scintillation detectors have been used in high-energy physics, nuclear physics, astrophysics, nuclear medicine, and other areas of radiation detection [9–12]; this created the conditions

for the invention of nuclear medicine imaging equipment, such as computed tomography (CT), positron emission tomography (PET), and single-photon emission computed tomography (SPECT).

In 1972, the first annular PET was designed using NaI (Tl) [13]; this PET was composed of 32 scintillation crystal detectors arranged in a ring structure. Since then, almost all PET scanners have had a ring structure because of its advantages in image reconstruction. In 1977, Budinger proposed for the first time the concept of time-of-flight PET (TOF-PET) [14], which can considerably improve the image quality by detecting the TOF of two photons generated by a coincidence event. In 1998, the first PET/CT system was developed [15]. This PET scanner was made of $\text{Bi}_4\text{Ge}_3\text{O}_{12}$ (BGO) crystals, and the CT scanner was employed to obtain an attenuation correction in order to achieve a better imaging quality.

Scintillation crystals are an important part of PET scanners, and their properties determine the performance of PET scanners. In this study, the principle of scintillation crystals and PET is presented, and possible developments of PET and scintillation crystals to be used in PET are proposed. The aim of this work is to guide researchers and engineers working in the PET field in selecting suitable scintillation crystals as well as to provide new ideas for designing scintillation crystals with better performance.

2. Basic Properties of Scintillation Crystals

Scintillation crystals used in PET are all inorganic scintillation crystals, which can convert high-energy (511 keV in PET) γ photons into a large number of fluorescent photons [16]. Then, the energy, time, and position information of the γ photons can be obtained through photoelectric sensors. The physical principle on which scintillation crystals are based is the photoelectric effect [17]. When high-energy γ photons pass through a scintillation crystal, the electrons inside the crystal are likely to be excited, and their energy levels transition to the excited state; then, the excited state decays through the emission of photons of a specific wavelength. The luminescence process of scintillation crystals can be simplified into three stages [18–21], as shown in Figure 1. In the first stage, the electrons inside the scintillation crystal are excited after interacting with high-energy γ photons, and the electron valence state transitions to the conduction band. At the same time, the same number of high-energy holes is generated, giving rise to high-energy electron–hole pairs; this is the process through which the energy is converted. In the second stage, the high-energy electron–hole pairs migrate toward the emission center inside the scintillation crystal and transfer energy to the luminescent center. This is the process through which the energy is transferred. However, the crystal contains internal defects, which act as hole and electron traps, resulting in a very-low-efficiency energy transfer. Therefore, it is usually necessary to add specific rare-earth elements inside scintillation crystals to improve their luminous efficiency [22]. In the third stage, the luminescent center is excited, the electrons are de-excited and are transferred from the conduction band to the valence band, and the excess energy is released in the form of photons. There are activators in the scintillation crystals to introduce additional energy levels within the bandgap to allow emission of light with energies below the bandgap and to avoid reabsorption of light by the scintillator material. It can be seen that there are several parameters that can be used for evaluating the performance of scintillation crystals, namely the stopping power, luminous properties, timing characteristics, and other properties.

2.1. Stopping Power

It can be seen from the luminescence process of scintillation crystals that the probability of a good scintillation crystal of reacting with γ photons should be as high as possible, which is beneficial to the improvement of the sensitivity of PET scanners. The stopping power indicates the ability of scintillation crystals to intercept γ photons [11]. To achieve a high stopping power, scintillation crystals should have a high density and a large effective atomic number (Z_{eff}). Although there are no concrete expressions of Z_{eff} , the effective atomic number for photoelectric absorption can be expressed as $Z_{\text{eff}} = (\sum w_i Z_i^4)^{1/4}$ [23],

where w_i and Z_i are the fraction of the total mass associated with the i^{th} element and the atomic number of the i^{th} element, respectively. For instance, BGO, Lu_2SiO_5 (LSO), and $\text{Lu}_{2(1-x)}\text{Y}_{2x}\text{SiO}_5$ (LYSO) are scintillation crystals with a high density, a large effective atomic number, and a high stopping power.

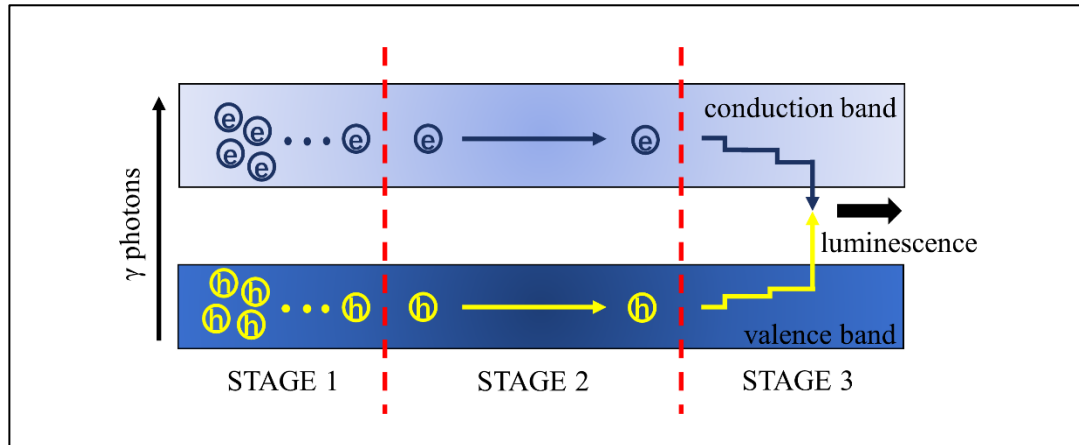


Figure 1. Luminescence process of scintillation crystals in PET.

2.2. Luminous Properties

The luminescent properties of scintillation crystals include the light output and the wavelengths of the emission spectrum [24]. The light output of scintillation crystals is an important parameter. A high light output signifies that under the same conditions, more fluorescent photons are generated, which improves the decoding precision and signal-to-noise ratio (SNR) of PET detectors. At the same time, scintillation crystals with a high light output also have a good energy resolution, which is beneficial for distinguishing the different energies of γ photons and neglect the γ photons redirected by the Compton scattering. LSO and LYSO are the most commonly used scintillation crystals with a high light output. In addition, LaBr_3 and $\text{Gd}_3(\text{Ga}, \text{Al})_5\text{O}_{12}$ (GAGG) exhibit an even higher light output and are considered to be the scintillation crystals with the greatest application potential in the future.

The maximum emission wavelength of the emission spectrum of scintillation crystals is also an important parameter; this wavelength is determined by the energy level transition of the luminescence process of scintillation crystals. The weak light signals produced by scintillation crystals are detected by photoelectric sensors. Photoelectric sensors are more sensitive at specific wavelengths; thus, it is important that the maximum emission wavelength matches the most sensitive wavelength of the sensor. Otherwise, the decoding precision and SNR ratio are significantly reduced. At present, Si photomultipliers (SiPMs) are the most commonly used photoelectric sensors; their most sensitive wavelength is 420 nm. LSO and LYSO are the best scintillation crystals with a maximum emission wavelength that can match that of SiPMs.

2.3. Timing Characteristics

Unlike CT, PET is a molecular imaging equipment that images a lesion by detecting pairs of γ photons generated by positron annihilation, which indicates that it is necessary to accurately measure the reaction time of each γ photon to determine whether two γ photons are produced by the same coincidence event. Therefore, PET scanners place high requirements on the timing characteristics of scintillation crystals. The timing characteristics of scintillation crystals consist of the signal rise time and the decay time [11]. The signal rise time represents the time that elapses between the moment in which the scintillation crystal detects γ photons and the moment in which fluorescent photons are generated. A shorter signal rise time indicates that the errors introduced in the time measurement of the γ photons are smaller, and thus the time resolution of the PET detector will be higher.

The SNR of the image will also be higher. At present, improving the time resolution is the most important research direction in PET. The decay time represents the time that elapses between the moment in which the scintillation crystal starts to generate fluorescent photons and the moment in which it stops generating them. If the decay time is sufficiently long, the luminous process generated by any γ photon will not be over by the time the subsequent γ photon generates another luminous process. As the two luminous processes are indistinguishable, considerable noise is created, which seriously affects the image quality. The signal rise time and the decay time are basically determined by two factors: One is the speed of the high-energy electron–hole pairs transferring from the ionization track to the emission center; the other is the lifetime of the luminescence state of the activator. Scintillation crystals with excellent timing characteristics, such as LSO, YSO, and LaBr₃, are preferred for PET detectors with a good time resolution.

2.4. Other Properties

There are also other important properties of scintillation crystals in PET; for instance, scintillation crystals used in PET scanners need to have a strong physical stability and an excellent chemical durability; otherwise, the processing and maintenance costs of the scintillation crystal will be very high. This requires that the scintillation crystal is not easily deliquescent and not easily oxidized. Scintillation crystals often work in a high-radiation environment, so they must exhibit a long luminous life, and the light output changes little with the environment [25]. Since the invention of PET, the scintillation crystals most extensively used have been NaI (Tl) [13], BGO [15], GSO [26], LSO [27], LYSO [28], LaBr₃ [29], and GAGG [30]. The basic properties of these crystals are listed in Table 1. LSO and LYSO are the scintillation crystals with the best overall performance. Compared with LSO, LYSO exhibits a lower spontaneous radiation [31] and has become the most commonly used scintillation crystal. Although new scintillation crystals, such as LaBr₃ and GAGG, have many performance advantages, they cannot replace LYSO due to the existence of several shortcomings.

Table 1. Basic properties of common scintillation crystals used in PET scanners.

Property	NaI (Tl)	BGO	GSO	LSO	LYSO	LaBr ₃	GAGG
Chemical Formula	NaI	Bi ₄ Ge ₃ O ₁₂	Gd ₂ SiO ₅	Lu ₂ SiO ₅	Lu _{2(1-x)} Y _{2x} SiO ₅	LaBr ₃	Gd ₃ (Ga, Al) ₅ O ₁₂
Z_{eff}	51	74	59	66	60	47	48
Density (g/cm ³)	3.67	7.13	4.89	7.4	7.2	5.3	6.63
Light output (ph/keV)	41	9	10	31	30	67	54
Wavelength (nm)	410	480	440	420	420	370	540
Decay time (ns)	230	300	60	40	41	25	94
Hygroscopic?	Yes	No	No	No	No	Yes	No

3. Basic Properties of PET Scanners

PET scanners realize imaging by detecting the position of the high-energy γ -photon pairs generated by the decay of the tracer (fluorodeoxyglucose (FDG) is the most commonly used tracer) injected into the organism [32,33]. As shown in Figure 2, a pair of γ photons originated from a coincidence event form a line of reaction (LOR), which contains information regarding the reaction site; then, metabolic images of the organism can be obtained by combining thousands of LORs through image reconstruction. Detectors are the core part of PET scanners [28], which are mainly composed of scintillation crystals and photoelectric sensors [34]. Scintillation crystals intercept high-energy γ photons and generate fluorescent photons; photoelectric sensors then detect the fluorescent photons and send the corresponding electrical signals to the electronic system to obtain the time, energy, and position information of the γ photons. The metabolic level and functional activity information can be obtained through image reconstruction [17], which can detect the presence of lesions earlier than magnetic resonance imaging (MRI) and CT scans [35,36]. The two most important parameters of PET scanners are their sensitivity and spatial resolution [37,38],

and the performance of scintillation crystals is directly related to the sensitivity and spatial resolution of PET scanners [28].

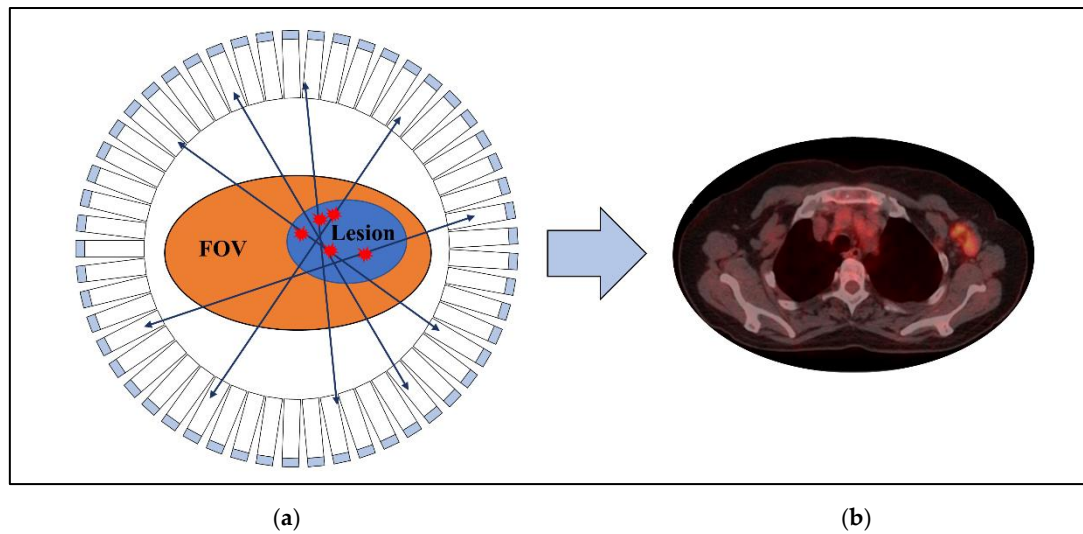


Figure 2. (a) Principle of PET scanner imaging, the circle composed of rectangles represents the detector blocks, the orange area represents the FOV, the blue area represents the lesion, the arrows represent the LORs; (b) example of a PET image after attenuation correction [39].

3.1. Sensitivity

The sensitivity of PET indicates the efficiency of detection of γ photons. A higher sensitivity of the PET scanner permits the dose of the FDG tracer injected into the patient and/or the scan time to be reduced [40]. To improve the sensitivity of PET, the scintillation crystal used in the PET scanner needs to have a high stopping power for γ photons, which means that the scintillation crystal is required to have a high effective atomic number and a high density [41]. The scintillation photons generated by the scintillation crystal are detected by photoelectric sensors, such as PMTs and SiPMs, which means that the scintillation crystal also needs to have a high light output [41], and its maximum emission wavelength needs to match the sensitive wavelength of the photodetectors. Additionally, if the flight time of a pair of γ photons originated from the same coincident event can be accurately measured, the location of the positron annihilation event can be more accurately determined, noise can be removed, and the effective sensitivity of the PET scanner can be improved [42]. This method is called TOF technology, and a higher light output is beneficial for increasing the TOF resolution. Most scintillation crystals are optically dense media, and many scintillation photons cannot be detected by photoelectric sensors due to total reflection; thus, the ideal scintillation crystal should have as low a refractive index as possible [43,44].

The stopping power is the most important attribute related to the sensitivity; BGO has a high effective atomic number and a high density; thus, it has a high stopping power for γ photons. However, PET scanners now rarely use BGO because of its low light output. LYSO and LSO have a slightly lower stopping power than BGO but an overall better performance; therefore, they have become the most commonly used scintillation crystals in PET.

3.2. Spatial Resolution

The spatial resolution indicates the sharpness of the PET image. The empirical expression to calculate the spatial resolution of PET is [45]:

$$R_{FWHM} = 1.25 \sqrt{(d/2)^2 + (0.0044R)^2 + s^2 + b^2 + \frac{(12.5r)^2}{r^2 + R^2}} \quad (1)$$

where R_{FWHM} is the full width at half maximum of the point spread function (PSF) of compact radioactive sources, representing the spatial resolution of the system; d is the size of the scintillation crystal; R is the radius of the PET scanner ring; s is the positron annihilation stroke, which is related to the type of isotope (the average annihilation path of positrons generated by ^{18}F in tissue fluid is approximately 0.5 mm); b is the error in the crystal decoding; r is the distance from LOR to the center of the ring; $(12.5r)^2/(r^2 + R^2)$ and the 1.25 coefficient represent the effects of the depth of interaction (DOI) and the image reconstruction on the system spatial resolution. The spatial resolution of the PET scanner is directly related to its geometric structure, and scintillation crystals with excellent performance can provide more degrees of freedom for the design of PET scanners.

The scintillation crystals used in high-spatial-resolution PET need to be easy to process; therefore, the size of the scintillation crystal can be very small, and the spatial resolution will be improved. For the same geometry of the PET scanner, the high decoding precision of the scintillation crystal position can improve the spatial resolution [46]. From this point of view, high-spatial-resolution PET scanners require scintillation crystals with a high light output and an emission spectrum that matches the sensitive wavelength of the photodetectors. PET scanners based on LSO or LYSO exhibit a high spatial resolution. With the continuous development of the biology and medicine fields, high-spatial-resolution PET is increasingly required, and consequently scintillation crystals with better performance are extensively investigated.

4. PET Development and Requirements of Scintillation Crystals

Current PET scanners are capable of attaining high-sensitivity images of lesions [17] and have a wide range of applications in the diagnosis of tumors [47–49], cardiovascular system diseases [50–52], and neurological diseases [53,54]. However, compared with other imaging equipment, such as CT and MRI, there is still room for improvement in the sensitivity and spatial resolution [41], and the inherent high cost of PET also restricts its widespread use. To improve the effective sensitivity and the spatial resolution of PET, the TOF technology and the DOI decoding have been proposed, and scintillation crystals exhibiting better performance promise to achieve a higher TOF and a higher DOI resolution. Depending on the object to be scanned, the future development of the PET technology mainly includes whole-body PET (Wb-PET), small-animal PET (SAP), and organ-specific PET. The functional requirements and system architectures of these PET scanners differ, as do the requirements of the corresponding scintillation crystals.

4.1. TOF-PET

Wb-PET has a radial field of view (FOV) greater than 60 cm [55–57], and the annihilation location can be anywhere in the 60 cm long LOR, which severely reduces the SNR of the image. TOF-PET was first proposed in 1977. As shown in Figure 3a, the TOF-PET scanner records the flight time of the γ -photon pair reaching the detector module. The probability of the annihilation event occurring at different positions along the LOR can be calculated; thus, the SNR of the reconstructed image of the system can be improved. The TOF technology improves the SNR of the image according to [42]:

$$\text{SNR}_{\text{TOF}} = \sqrt{\frac{2D}{c\Delta t}} \text{SNR}_{\text{non-TOF}} \quad (2)$$

where SNR_{TOF} and $\text{SNR}_{\text{non-TOF}}$ represent the SNR of PET with and without the TOF technology, respectively; D represents the length of the LOR; c represents the speed of light; Δt represents the coincidence time resolution (CTR). The CTR in TOF-PET is determined by the time resolution of scintillation crystals and the time error of electronic system. TOF-PET scanners with a high SNR of the images [58] also offer the following advantages: Improved image quality in larger patients, reduced isotope radiation dose, ultralow-dose imaging and measurements, improved image quality in case of missing data, and greater convergence speed of the image reconstruction algorithm.

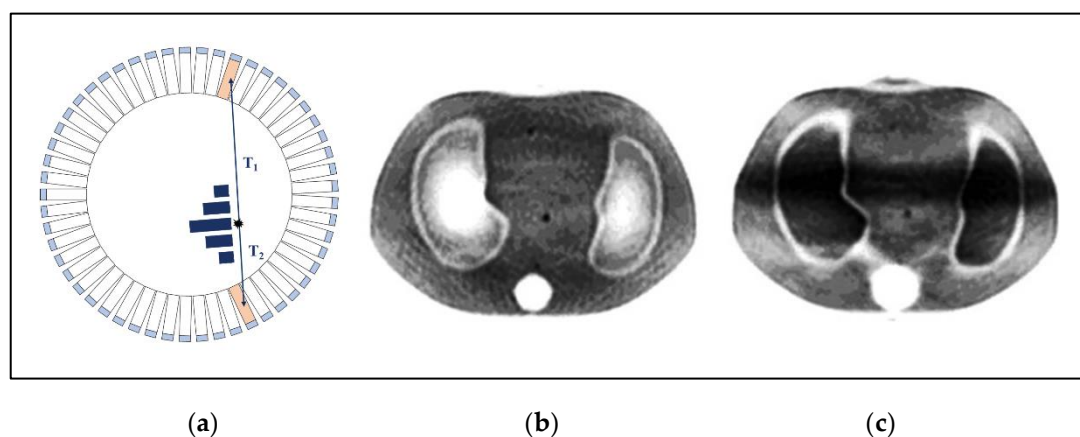


Figure 3. (a) Principle of TOF-PET. PET phantom images after (b) TOF reconstruction and (c) non-TOF reconstruction [58].

TOF-PET requires an electronic system with a high time-measurement resolution and scintillation crystals with good timing characteristics. At present, the scintillation crystals most commonly used in commercial TOF-PET scanners are LSO and LYSO. Scintillation crystals with good timing characteristics need to have an extremely fast rise signal, a short decay time, and a high light output [59]. Currently, LaBr₃ may be the most suitable scintillation crystal to improve the TOF resolution of PET scanners [60–62]. Indeed, a 77 ps TOF resolution for an LaBr₃ crystal with dimensions of 6 × 6 × 6 mm³ has been reported [63], and the obtained 6.4% energy resolution is considerably higher than that of LYSO. A 132.9 ps TOF resolution for an LSO crystal of the same size and a 129 ps TOF resolution for an LYSO of the same size have also been reported, and the corresponding energy resolutions are 10.4% and 8.9%, respectively. The performance of an LaBr₃-based PET scanner has also been tested [64], and the obtained 375 ps CTR is superior to that achieved in commercial TOF-PET scanners (550–600 ps). Indeed, LaBr₃ has extremely good timing characteristics, but it has not become the mainstream choice of scintillation crystals used in TOF-PET because of its deliquescence. With the development of scintillation crystals, the CTR of TOF-PET will certainly be improved further.

4.2. DOI-PET

To observe the physiological response and metabolic process of small animals quantitatively and dynamically, PET scanners need to have a high spatial resolution, so they can have a wide range of applications in the oncology, neurology, and pharmaceutical industry fields [65–67]. However, in high-resolution PET scanners, as shown in Figure 4, the parallax errors caused by the DOI are significant [68,69].

In a system with a given DOI resolution w , if only the size of the scintillation crystal and the size of the scanner are considered, the radial resolution at any given point within the FOV can be estimated as follows [70]:

$$\Gamma \approx \sqrt{\left(\frac{d}{2}\right)^2 + \frac{(w^2 - d^2)}{4R^2}r^2} \quad (3)$$

To reduce the effects of the DOI, the detectors in PET need to have the ability to calculate the depth position of the γ photons; in this way, the LORs can be positioned more accurately. Additionally, simulation studies have demonstrated that high-resolution DOI decoding also improves the SNR of the image [71]. Currently, the main DOI decoding methods in PET scanners include the multilayer [72,73], dual-ended readout [74], and light-sharing [75,76] methods. Although the structures of these DOI detectors are different, they all require scintillation crystals with a high light output to improve the DOI decoding resolution.

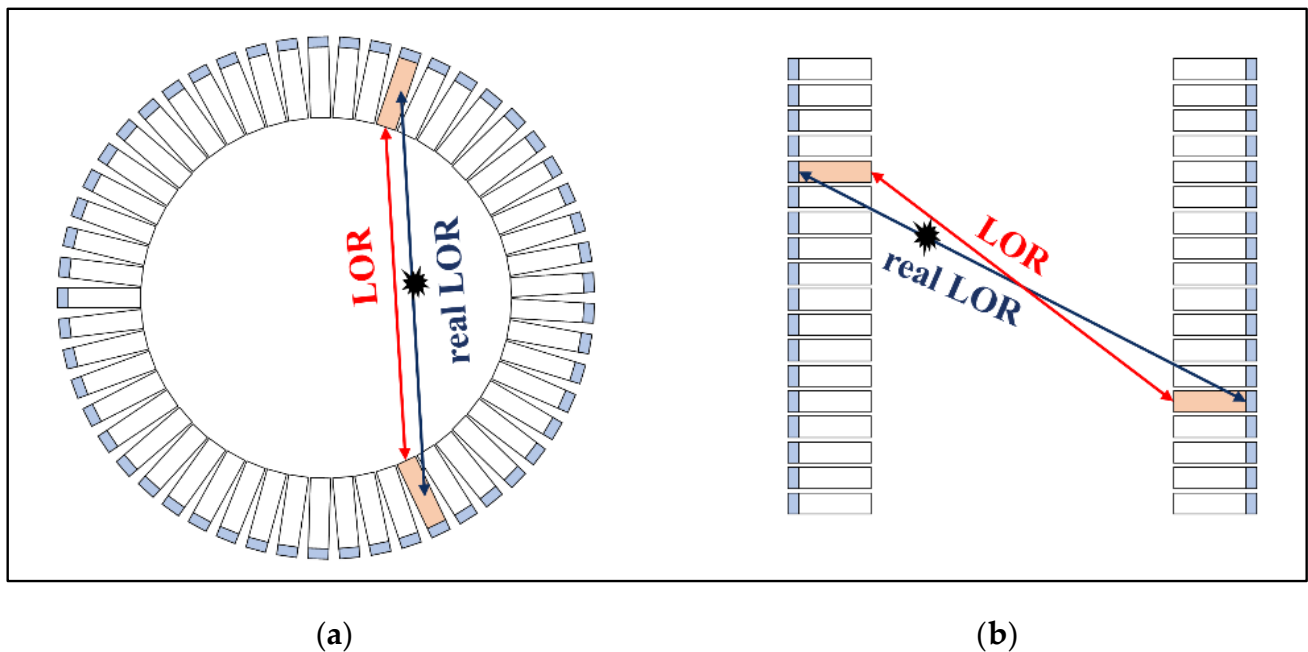


Figure 4. (a) Parallax error in the LOR in the radial direction caused by the DOI; (b) Parallax error in the LOR in the axial direction caused by the DOI.

LYSO and LSO are the most commonly used scintillation crystals in PET; DOI resolutions of 1.9 ± 0.1 mm and 1.76 ± 0.13 mm have been reported for an LSO crystal with dimensions of $1.5 \times 1.5 \times 20$ mm³ and an LYSO crystal with dimensions of $0.62 \times 0.62 \times 20$ mm³, respectively [74,77]. In recent studies, it has been found that GAGG with a high light output and no spontaneous radiation can achieve a higher DOI resolution [78,79]. Choghadi et al., [80] reported a DOI resolution of 1.2 ± 0.08 mm for a GAGG crystal with dimensions of $1.2 \times 1.2 \times 20$ mm³ using the dual-ended readout method, and the corresponding energy resolution is $12.4\% \pm 0.6\%$, which is acceptable. The DOI resolution of GAGG is higher than that of LYSO and LSO and closer to the size of the crystal. Thus, the DOI factor for GAGG can be little, which indicates that GAGG has the potential to further improve the spatial resolution of PET scanners in the future.

4.3. Wb-PET

The most important function of PET is imaging the metabolic processes of the human body to monitor human health. The structure of the Wb-PET scanners comprises a ring of detectors, as shown in Figure 5a, and the axial FOV (AFOV) of the Wb-PET scanners currently in use is generally 20–30 cm [55–57]. Data is acquired by moving the patient, and multiple tomographic images are stitched together into a whole-body image. The sensitivity of the system is low because the geometric angle covered by the detector is small; furthermore, the scan time is at least 20 min, and imaging multiple organs simultaneously can be difficult. To solve this problem, the concept of a long-AFOV PET was proposed [81]; its working principle is illustrated in Figure 5b. The first studies on the uEXPLORER total-body PET scanner on human subjects were performed in 2019 [82]. With an AFOV of 194 cm, the uEXPLORER total-body PET scanner can obtain high-quality dynamic metabolic images of the entire human body in less than 2 min. Furthermore, the sensitivity, SNR, and imaging FOV of the long-AFOV PET are far superior to those of traditional Wb-PET scanners. The long-AFOV PET is likely to be the future direction of human-body PET.

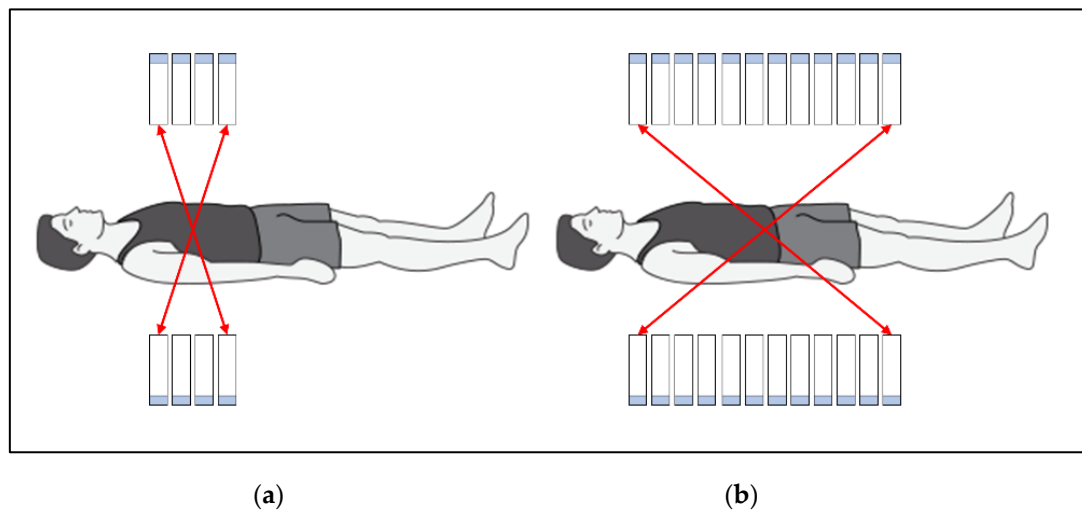


Figure 5. (a) Scanning field of the traditional Wb-PET scanners and (b) scanning field of the long-AFOV PET.

The long-AFOV PET scanner has a greater axial length than the traditional Wb-PET scanners; thus, the LOR position error caused by the axial DOI is also larger, which means that scintillation crystals should have a perfect performance regarding both the time resolution and the DOI decoding. Theoretical studies have shown that the sensitivity and image quality of the long-AFOV PET with both 320 ps TOF and 4 mm DOI are more than four times those of the long-AFOV PET without the TOF and DOI technologies [71]. LSO and LYSO are considered to be the most suitable scintillation crystals, and almost all Wb-PET scanners use LSO or LYSO. However, the cost of the LSO and LYSO crystals is very high, and cheaper scintillation crystals, such as BGO or GSO, could be considered for the long-AFOV PET scanner [83]; however, this leads to a compromise in the spatial resolution and the sensitivity of PET scanners. The scintillation crystals most commonly used in commercial Wb-PET scanners are listed in the Table 2 alongside their respective properties.

Table 2. Scintillation crystals used in WB-PET and their properties.

Crystal Material	Crystal Size (mm ³)	Array Structure	DOI?	CTR (ps)	Spatial Resolution (mm)	Sensitivity (kcps/MBq)	Name
LYSO	2.76 × 2.76 × 18.1	5 × 14	Yes	412	~3.0	174	uEXPLORER [84–86]
LYSO	3.2 × 3.2 × 20	5 × 5	No	210	~3.5	16.4	Biograph Vision [87]
LSO	4 × 4 × 20	13 × 13	No	N/A	~4.7	N/A	Biograph Horizon [88]
LYSO	3.95 × 5.3 × 25	4 × 9	No	381.7	~4.6	13.3	Discovery MI [89,90]
LYSO	4.2 × 6.3 × 25	6 × 9	No	552.7	~4.6	6.3	Discovery MI-DR [90,91]
LYSO	4 × 4 × 22	23 × 44	No	585	~4.8	6.6	Gemini TF [92]

4.4. SAP

Imaging of metabolic processes in small animals using PET has a wide range of applications in the oncology, neurology, and pharmaceutical industry fields [65–67]. It is necessary to develop dedicated high-resolution SAP scanners because Wb-PET scanners are too large and expensive for small-animal imaging and exhibit a low sensitivity and a poor spatial resolution [93]. In 1992, the first SAP scanner called RAT-PET was launched by CTI (US), using BGO crystals with dimensions of 2.4 × 2.4 × 4.6 mm³. In 1999, an SAP scanner with a diameter of 17.2 cm using LSO crystals was developed, which achieved

a spatial resolution of $1.8 \times 1.8 \times 1.8 \text{ mm}^3$ and an absolute sensitivity of 0.56% [94]. To achieve high-spatial-resolution SAP scanners, small-sized scintillation crystals need to be used, which means that the scintillation crystals need to have good processing properties. Clearly, the size of the scintillation crystal cannot be too small, and it should match the decoding precision of the detector. The DOI affects considerably the spatial resolution in SAP; therefore, currently used SAP scanners often possess a DOI decoding ability, which enables them to achieve a high spatial resolution. SAP does not need the TOF technology because the radial FOV of SAP is much smaller than that of Wb-PET; furthermore, it is unclear how the TOF technology could improve the SNR of the images. Table 3 lists the crystals most typically used in SAP and their properties.

Table 3. Scintillation crystals used in SAP and their properties.

Crystal Material	Crystal Size (mm^3)	Array Specification	DOI?	Spatial Resolution (mm)	Sensitivity	Name
GSO	$2 \times 2 \times 10$	N/A	No	2.32	2.83%	Mosaic HP [95]
LYSO/LuYAP	$2 \times 2 \times 10$	$8 \times 8/8 \times 8$	Yes	1.94	3.03%	ClearPET [96]
BGO	$2.32 \times 2.32 \times 9.4$	8×8	No	2	5.90%	FLEX Triumph [97]
LYSO	$1.89 \times 1.89 \times 13$	13×13	No	1	2.04%	Trans-PET [98]
NaI(Tl)	$51 \times 38 \times 9.5$	Continuous	Yes	0.55	0.20%	U-PET [99]
LYSO	$25.4 \times 25.4 \times 8$	Continuous	Yes	0.85	12.60%	Beta_CUBE [100]

4.5. Organ-Specific PET

There are also several other PET scanners for inspecting specific organs; the most common and effective of these are brain-PET and dedicated-breast PET (Db-PET) scanners. The only commercially available brain-PET is the HRRT-PET developed by Siemens [101,102]; however, this system has been discontinued for various reasons. Recent studies have shown that PET can be used as a diagnostic tool for neurological diseases, such as Alzheimer's disease [103], Parkinson's disease [104], and epilepsy [105]. Brain-PET also consists of a ring-like structure, but it covers only the head of the human body; thus, it has a better sensitivity and a greater spatial resolution for the brain than Wb-PET. The diagnosis of brain diseases and brain research require a high image quality, so it is necessary for brain-PET to achieve a high TOF resolution and a high DOI decoding resolution. LSO and LYSO are currently the best scintillation crystals also in the case of brain-PET scanners. Brain-PET scanners have a simpler structure than Wb-PET scanners. Thus, implementing brain-PET scanners based on difficult-to-process scintillation crystals, such as LaBr_3 , could provide high-quality images for brain science research and neurological research, which also have the potential to develop in the future. Table 4 presents some of the crystals used in brain-PET scanners and their properties.

Table 4. Scintillation crystals used in brain-PET and their properties.

Crystal Material	Crystal Size (mm^3)	Array Structure	DOI?	TOF?	Spatial Resolution (mm)	Sensitivity	Name
GSO	$4.9 \times 5.9 \times 8$	11×8	Yes	Yes	~4.0	0.72%	PET-Hat [106]
LSO/LYSO	$2.44 \times 2.44 \times 10$	8×8	Yes	No	~3.0	0.5%	HRRT [101,102]
LYSO	$1.5 \times 1.5 \times 10$	32×33	No	No	2–4	0.5%	Helmet-PET [107]
LYSO	$3 \times 3 \times 10$	10×10	No	No	N/A	N/A	Mind-tracker [108]

Breast cancer is the most common malignant tumor in women, but early breast cancer may not be visible in a Wb-PET scan [109]. To overcome this limitation, several Db-PET scanners have emerged nowadays aiming to improve the spatial resolution and sensitivity of breast imaging. The scan mode of Db-PET scanners is different from that of normal PET scanners; the patient is either sitting or lying prone with the breast in the center of the FOV. Most of Db-PET scanners are characterized by a double-plate structure, and each plate

consists of multiple detector modules. TOF and DOI are not required to improve the image quality. Table 5 lists some of the crystals used in Db-PET scanners and their properties.

Table 5. Scintillation crystals used in Db-PET and their properties.

Crystal Material	Size (mm ³)	Array	Planar Detector (cm)	Spatial Resolution (mm)	Relative Sensitivity	Name
LGSO	3 × 3 × 10	20 × 30	15 × 20	4.1	5%	PET Mammography [110]
LSO	3 × 3 × 20	9 × 9	40 × 30	N/A	N/A	DbPET/CT [111]
LYSO	2 × 2 × 15	96 × 72	12 × 20	~2	6.88%	PEM/PET [112]

5. Conclusions

Since the discovery of NaI (Tl), the PET technology has gradually developed, and the currently used PET scanners mainly use LSO or LYSO crystals in combination with SiPMs for detectors. PET scanners are often combined with CT or MRI scanners to perform multimodal imaging; they play an important role in the diagnosis of tumors, neurological diseases, and cardiovascular diseases and have wide application in the biopharmaceutical industry, scientific research, and other fields. At present, the predominant limitations of PET scanners include their low sensitivity, low spatial resolution, and high cost.

To improve the effective sensitivity, the TOF technology has been widely investigated in PET research; furthermore, LaBr₃ and other scintillation crystals are believed to be able to further improve the CTR of TOF-PET. In addition, with the development of the pharmaceutical industry, brain science research, and neuroscience research, ultra-high-resolution PET has the potential to make a breakthrough in these fields. GAGG exhibits a better energy resolution, a superior light output, and no spontaneous radiation compared with LYSO. In a recent study [30,78,79], PET detectors using GAGG crystals have been found to possess a very high decoding precision. LaBr₃ and GAGG have a greater light output than LYSO; therefore, it may be possible to obtain a PET scintillation crystal with better comprehensive performance by further improving the light output of LYSO scintillation crystals. Although the long-AFOV PET exhibits a great performance, its high cost limits its widespread use, which brings cheaper and less powerful scintillation crystals, such as BGO and GSO, back into consideration.

It will be very difficult to find an ideal scintillation crystal for all PET scanners within a short time, and the design of each individual PET scanner should be based on the functional requirements, reaching compromises in terms of the sensitivity, spatial resolution, and cost, and the selection of an appropriate scintillation crystal. Clearly, researchers and engineers in the PET field also expect the discovery of scintillation crystals with enhanced performance. At present, if a scintillation crystal with a light output greater than 100 ph/keV and a decay time less than 5 ns is found on the basis of LYSO, the performance of PET scanners can be significantly improved, and this is what researchers in the PET field have been working on.

Author Contributions: Methodology, X.Z.; investigation, H.Z.; writing—original draft preparation, X.Y.; writing—review and editing, H.P.; J.X.; Q.P.; S.X.; funding acquisition, Q.R. All authors have read and agreed to the published version of the manuscript.

Funding: This work was supported by the Shenzhen Science and Technology Program (JCYJ20200109140603831, RCBS20200714114920148, KQTD20180412181221912), the Guangdong Basic and Applied Basic Research Foundation (2020A15110588), State Key Lab of Digital Manufacturing Equipment & Technology Open Project Funding Project (DMETKF2022020), the Nanshan District Science and Technology Program (LHTD20190009). We sincerely thank the Micro and Nano Fabrication and Measurement Laboratory of Mechanical Science and Engineering in HUST.

Institutional Review Board Statement: Not applicable.

Informed Consent Statement: Not applicable.

Data Availability Statement: Not applicable.

Conflicts of Interest: The authors declare no conflict of interest.

References

1. Kawano, N.; Shinozaki, K.; Nakauchi, D.; Kimura, H.; Yanagida, T. Scintillation properties of organic–inorganic layered perovskite nanocrystals in glass. *J. Appl. Phys.* **2020**, *127*, 213103. [[CrossRef](#)]
2. Xu, Q.; Wang, J.; Shao, W.; Ouyang, X.; Wang, X.; Zhang, X.; Guo, Y.; Ouyang, X. A solution-processed zero-dimensional all-inorganic perovskite scintillator for high resolution gamma-ray spectroscopy detection. *Nanoscale* **2020**, *12*, 9727–9732. [[CrossRef](#)] [[PubMed](#)]
3. Van Eijk, C.W. Development of inorganic scintillators. *Nucl. Instrum. Methods Phys. Res. Sect. A Accel. Spectrometers Detect. Assoc. Equip.* **1997**, *392*, 285–290. [[CrossRef](#)]
4. Crookes, W.; Dewar, J. Note on the effect of extreme cold on the emanations of radium. *Proc. R. Soc. Lond.* **1904**, *72*, 69–71.
5. Moon, R.J. Inorganic crystals for the detection of high energy particles and quanta. *Phys. Rev.* **1948**, *73*, 1210. [[CrossRef](#)]
6. Hofstadter, R. The detection of gamma-rays with thallium-activated sodium iodide crystals. *Phys. Rev.* **1949**, *75*, 796. [[CrossRef](#)]
7. Hofstadter, R. Alkali halide scintillation counters. *Phys. Rev.* **1948**, *74*, 100. [[CrossRef](#)]
8. Seliger, H.H. A photoelectric method for the measurement of spectra of light sources of rapidly varying intensities. *Anal. Biochem.* **1960**, *1*, 60–65. [[CrossRef](#)]
9. Gektin, A.; Korzhik, M. *Inorganic Scintillators for Detector Systems*; Springer: Berlin, Germany, 2017.
10. Lecoq, P. Development of new scintillators for medical applications. *Nucl. Instrum. Methods Phys. Res. Sect. A Accel. Spectrometers Detect. Assoc. Equip.* **2016**, *809*, 130–139. [[CrossRef](#)]
11. Weber, M.J. Inorganic scintillators: Today and tomorrow. *J. Lumin.* **2002**, *100*, 35–45. [[CrossRef](#)]
12. Williams, R.T.; Grim, J.Q.; Li, Q.; Ucer, K.B.; Bizarri, G.A.; Burger, A. Scintillation Detectors of Radiation: Excitations at High Densities and Strong Gradients. In *Excitonic and Photonic Processes in Materials*; Springer: Singapore, 2015; pp. 299–358.
13. Robertson, J.S.; Marr, R.B.; Rosenblum, M.; Radeka, V.; Yamamoto, Y.L. *32-Crystal Positron Transverse Section Detector (No. BNL-17237; CONF-720959-1)*; Brookhaven National Lab.: Upton, NY, USA, 1972.
14. Budinger, T.F. Instrumentation trends in nuclear medicine. *Semin. Nucl. Med.* **1977**, *7*, 285–297. [[CrossRef](#)]
15. Kinahan, P.E.; Townsend, D.W.; Beyer, T.; Sashin, D. Attenuation correction for a combined 3D PET/CT scanner. *Med. Phys.* **1998**, *25*, 2046–2053. [[CrossRef](#)] [[PubMed](#)]
16. Blasse, G. Scintillator materials. *Chem. Mater.* **1994**, *6*, 1465–1475. [[CrossRef](#)]
17. Muehlehner, G.; Karp, J.S. Positron emission tomography. *Phys. Med. Biol.* **2006**, *51*, R117. [[CrossRef](#)]
18. Bizarri, G. Scintillation mechanisms of inorganic materials: From crystal characteristics to scintillation properties. *J. Cryst. Growth* **2010**, *312*, 1213–1215. [[CrossRef](#)]
19. Nikl, M. Scintillation detectors for X-rays. *Meas. Sci. Technol.* **2006**, *17*, R37. [[CrossRef](#)]
20. Nikl, M.; Yoshikawa, A. Recent R&D trends in inorganic single-crystal scintillator materials for radiation detection. *Adv. Opt. Mater.* **2015**, *3*, 463–481.
21. Bartram, R.H.; Lempicki, A. Efficiency of electron-hole pair production in scintillators. *J. Lumin.* **1996**, *68*, 225–240. [[CrossRef](#)]
22. Rodnyi, P.A. *Physical Processes in Inorganic Scintillators*; CRC Press: Boca Raton, FL, USA, 1997; Volume 14.
23. Yanagida, T. Inorganic scintillating materials and scintillation detectors. *Proc. Jpn. Acad. Ser. B* **2018**, *94*, 75–97. [[CrossRef](#)] [[PubMed](#)]
24. Derenzo, S.E.; Weber, M.J.; Bourret-Courchesne, E.; Klintonberg, M.K. The quest for the ideal inorganic scintillator. *Nucl. Instrum. Methods Phys. Res. Sect. A Accel. Spectrometers Detect. Assoc. Equip.* **2003**, *505*, 111–117. [[CrossRef](#)]
25. Guo, L.; Tian, J.; Chen, P.; Derenzo, S.E.; Choong, W.S. Improving timing performance of double-ended readout in TOF-PET detectors. *J. Instrum.* **2020**, *15*, P01003. [[CrossRef](#)]
26. Yamamoto, S.; Ishibashi, H. A GSO depth of interaction detector for PET. *IEEE Trans. Nucl. Sci.* **1998**, *45*, 1078–1082. [[CrossRef](#)]
27. Melcher, C.L. Lutetium orthosilicate single crystal scintillator detector. U.S. Patent 5,025,151, 18 June 1991.
28. Lewellen, T.K. Recent developments in PET detector technology. *Phys. Med. Biol.* **2008**, *53*, R287. [[CrossRef](#)]
29. Van Loef, E.V.D.; Dorenbos, P.; Van Eijk, C.W.E.; Krämer, K.; Güdel, H.U. High-energy-resolution scintillator: Ce³⁺ activated LaBr₃. *Appl. Phys. Lett.* **2001**, *79*, 1573–1575. [[CrossRef](#)]
30. Kamada, K.; Yanagida, T.; Endo, T.; Tsutumi, K.; Usuki, Y.; Nikl, M.; Fujimoto, Y.; Fukabori, A.; Yoshikawa, A. 2 inch diameter single crystal growth and scintillation properties of Ce: Gd₃Al₂Ga₃O₁₂. *J. Cryst. Growth* **2012**, *352*, 88–90. [[CrossRef](#)]
31. Yao, B.; Zheng, L.; Zhao, G.; Zong, Y. Judd-Ofelt Analysis of Spectroscopic Properties of Tm³⁺ Doped Lu₂SiO₅ Crystals. *Chin. J. Lasers* **2008**, *35*, 601.
32. Jadvar, H. Prostate cancer: PET with 18F-FDG, 18F-or 11C-acetate, and 18F-or 11C-choline. *J. Nucl. Med.* **2011**, *52*, 81–89. [[CrossRef](#)]
33. Deng, X.; Rong, J.; Wang, L.; Vasdev, N.; Zhang, L.; Josephson, L.; Liang, S.H. Chemistry for positron emission tomography: Recent advances in 11C, 18F, 13N, and 15O labeling reactions. *Angew. Chem. Int. Ed.* **2019**, *58*, 2580–2605. [[CrossRef](#)]
34. Xie, S.; Chen, J.; Yang, M.; Shi, H.; Peng, Q.; Xu, J. A γ -photon detector based on liquid light guide for whole-body PET. *J. Instrum.* **2017**, *12*, P11012. [[CrossRef](#)]

35. Yang, H.L.; Liu, T.; Wang, X.M.; Xu, Y.; Deng, S.M. Diagnosis of bone metastases: A meta-analysis comparing 18FDG PET, CT, MRI and bone scintigraphy. *Eur. Radiol.* **2011**, *21*, 2604–2617. [[CrossRef](#)]
36. McGeer, P.L.; Kamo, H.; Harrop, R.; McGeer, E.G.; Martin, W.R.W.; Pate, B.D.; Li, D.K.B. Comparison of PET, MRI, and CT with pathology in a proven case of Alzheimer's disease. *Neurology* **1989**, *36*, 1569. [[CrossRef](#)]
37. Sanaat, A.; Arabi, H.; Ay, M.R.; Zaidi, H. Novel preclinical PET geometrical concept using a monolithic scintillator crystal offering concurrent enhancement in spatial resolution and detection sensitivity: A simulation study. *Phys. Med. Biol.* **2020**, *65*, 045013. [[CrossRef](#)]
38. Visser, E.P.; Disselhorst, J.A.; Brom, M.; Laverman, P.; Gotthardt, M.; Oyen, W.J.; Boerman, O.C. Spatial resolution and sensitivity of the Inveon small-animal PET scanner. *J. Nucl. Med.* **2009**, *50*, 139–147. [[CrossRef](#)]
39. Ming, Y.; Wu, N.; Qian, T.; Li, X.; Wan, D.Q.; Li, C.; Li, Y.; Wu, Z.; Wang, X.; Liu, J.; et al. Progress and future trends in PET/CT and PET/MRI molecular imaging approaches for breast cancer. *Front. Oncol.* **2020**, *10*, 1301. [[CrossRef](#)] [[PubMed](#)]
40. Eriksson, L.; Townsend, D.; Conti, M.; Eriksson, M.; Rothfuss, H.; Schmand, M.; Casey, M.E.; Bendriem, B. An investigation of sensitivity limits in PET scanners. *Nucl. Instrum. Methods Phys. Res. Sect. A Accel. Spectrometers Detect. Assoc. Equip.* **2007**, *580*, 836–842. [[CrossRef](#)]
41. Peng, H.; S Levin, C. Recent developments in PET instrumentation. *Curr. Pharm. Biotechnol.* **2010**, *11*, 555–571. [[CrossRef](#)] [[PubMed](#)]
42. Dahlbom, M. PET Imaging: Basic and New Trends. In *Handbook of Particle Detection and Imaging*; Springer International Publishing: Cham, Switzerland, 2021; pp. 1237–1277.
43. Salomoni, M.; Pots, R.; Auffray, E.; Lecoq, P. Enhancing light extraction of inorganic scintillators using photonic crystal. *Crystals* **2018**, *8*, 78. [[CrossRef](#)]
44. Pots, R.H.; Salomoni, M.; Gundacker, S.; Zanettini, S.; Gâté, V.; Usureau, E.; Turover, D.; Lecoq, P.; Auffray, E. Improving light output and coincidence time resolution of scintillating crystals using nanoimprinted photonic crystal slabs. *Nucl. Instrum. Methods Phys. Res. Sect. A Accel. Spectrometers Detect. Assoc. Equip.* **2019**, *940*, 254–261. [[CrossRef](#)]
45. Moses, W.W. Fundamental limits of spatial resolution in PET. *Nucl. Instrum. Methods Phys. Res. Sect. A Accel. Spectrometers Detect. Assoc. Equip.* **2011**, *648*, S236–S240. [[CrossRef](#)]
46. Zhang, X.; Yu, H.; Xie, Q.; Xie, S.; Ye, B.; Guo, M.; Zhao, Z.; Huang, Q.; Xu, J.; Peng, Q. Design study of a PET detector with 0.5 mm crystal pitch for high-resolution preclinical imaging. *Phys. Med. Biol.* **2021**, *66*, 135013. [[CrossRef](#)] [[PubMed](#)]
47. Mintun, M.A.; Welch, M.J.; Siegel, B.A.; Mathias, C.J.; Brodack, J.W.; McGuire, A.H.; Katzenellenbogen, J.A. Breast cancer: PET imaging of estrogen receptors. *Radiology* **1988**, *169*, 45–48. [[CrossRef](#)]
48. Coleman, R.E. PET in lung cancer. *J. Nucl. Med.* **1999**, *40*, 814–820.
49. Enghardt, W.; Crespo, P.; Fiedler, F.; Hinz, R.; Parodi, K.; Pawelke, J.; Poenisch, F. Charged hadron tumour therapy monitoring by means of PET. *Nucl. Instrum. Methods Phys. Res. Sect. A Accel. Spectrometers Detect. Assoc. Equip.* **2004**, *525*, 284–288. [[CrossRef](#)]
50. Schindler, T.H.; Schelbert, H.R.; Quercioli, A.; Dilsizian, V. Cardiac PET imaging for the detection and monitoring of coronary artery disease and microvascular health. *JACC Cardiovasc. Imaging* **2010**, *3*, 623–640. [[CrossRef](#)]
51. Phelps, M.E. *PET: Molecular Imaging and its Biological Applications*; Springer Science Business: Media, UK, 2004.
52. Bengel, F.M.; Schwaiger, M. Assessment of cardiac sympathetic neuronal function using PET imaging. *J. Nucl. Cardiol.* **2004**, *11*, 603–616. [[CrossRef](#)] [[PubMed](#)]
53. Nordberg, A.; Rinne, J.O.; Kadir, A.; Långström, B. The use of PET in Alzheimer disease. *Nat. Rev. Neurol.* **2010**, *6*, 78. [[CrossRef](#)]
54. Younes-Mhenni, S.; Janier, M.-F.; Cinotti, L.; Antoine, J.C.; Tronc, F.; Cottin, V.; Ternamian, P.J.; Trouillas, P.; Honnorat, J. FDG-PET improves tumour detection in patients with paraneoplastic neurological syndromes. *Brain* **2004**, *127*, 2331–2338. [[CrossRef](#)]
55. Bettinardi, V.; Danna, M.; Savi, A.; Lecchi, M.; Castiglioni, I.; Gilardi, M.C.; Bammer, H.; Lucignani, G.; Fazio, F. Performance evaluation of the new whole-body PET/CT scanner: Discovery ST. *Eur. J. Nucl. Med. Mol. Imaging* **2004**, *31*, 867–881. [[CrossRef](#)]
56. Surti, S.; Karp, J.S. Imaging characteristics of a three-dimensional GSO whole-body PET camera. *J. Nucl. Med.* **2004**, *45*, 1040–1049.
57. Jakoby, B.W.; Bercier, Y.; Conti, M.; Casey, M.E.; Bendriem, B.; Townsend, B.W. 2011 Physical and clinical performance of the mCT time-of-flight PET/CT scanner. *Phys. Med. Biol.* **2011**, *56*, 2375. [[CrossRef](#)]
58. Conti, M. Why is TOF PET reconstruction a more robust method in the presence of inconsistent data? *Phys. Med. Biol.* **2010**, *56*, 155. [[CrossRef](#)]
59. Lecoq, P.; Auffray, E.; Brunner, S.; Hillemanns, H.; Jarron, P.; Knapitsch, A.; Meyer, T.; Powolny, F. Factors influencing time resolution of scintillators and ways to improve them. *IEEE Trans. Nucl. Sci.* **2010**, *57*, 2411–2416. [[CrossRef](#)]
60. Vinke, R.; Seifert, S.; Schaart, D.R.; Schreuder, F.P.; de Boer, M.R.; van Dam, H.T.; Beekman, F.J.; Löhner, H.; Dendooven, P. Optimization of digital time pickoff methods for LaBr 3-SiPM TOF-PET detectors. In Proceedings of the 2009 IEEE Nuclear Science Symposium Conference Record (NSS/MIC), Orlando, FL, USA, 24 October–1 November 2009; IEEE, 2009; pp. 2962–2968.
61. Kuhn, A.; Surti, S.; Karp, J.S.; Raby, P.S.; Shah, K.S.; Perkins, A.E.; Muehlethner, G. Design of a lanthanum bromide detector for time-of-flight PET. *IEEE Trans. Nucl. Sci.* **2004**, *51*, 2550–2557. [[CrossRef](#)]
62. Karp, J.S.; Wiener, R.; Surti, S.; Schmall, J.P.; Ferri, A.; Gola, A.; Tarolli, A.; Piemonte, C. Timing and energy resolution of new near-UV SiPMs coupled to LaBr₃: Ce for TOF-PET. In Proceedings of the 2013 IEEE Nuclear Science Symposium and Medical Imaging Conference (2013 NSS/MIC), Seoul, Korea, 27 October–2 November 2013; pp. 1–5.
63. Xie, S.; Zhang, X.; Zhang, Y.; Ying, G.; Huang, Q.; Xu, J.; Peng, Q. Evaluation of various scintillator materials in radiation detector design for positron emission tomography (PET). *Crystals* **2020**, *10*, 869. [[CrossRef](#)]

64. Daube-Witherspoon, M.E.; Surti, S.; Perkins, A.; Kyba, C.C.; Wiener, R.; Werner, M.E.; Kulp, R.; Karp, J.S. The imaging performance of a LaBr₃-based PET scanner. *Phys. Med. Biol.* **2009**, *55*, 45. [[CrossRef](#)]
65. Liu, T.; Liu, C.; Xu, X.; Liu, F.; Guo, X.; Li, N.; Wang, X.; Yang, J.; Yang, X.; Zhu, H.; et al. Preclinical Evaluation and Pilot Clinical Study of Al18F-PSMA-BCH for Prostate Cancer PET Imaging. *J. Nucl. Med.* **2019**, *60*, 1284–1292. [[CrossRef](#)]
66. Miao, Z.; Ren, G.; Liu, H.; Jiang, L.; Cheng, Z. Small-animal PET imaging of human epidermal growth factor receptor positive tumor with a ⁶⁴Cu labeled affibody protein. *Bioconjugate Chem.* **2010**, *21*, 947–954. [[CrossRef](#)]
67. Epstein, F.H.; Catana, C.; Tsui, B.M.; Ritman, E.L. Small-animal molecular imaging methods. *J. Nucl. Med. Off. Publ. Soc. Nucl. Med.* **2010**, *51*, 18S–32S.
68. Sanchez, F.; Moliner, L.; Correcher, C.; Gonzalez, A.; Orero, A.; Carles, M.; Soriano, A.; Rodriguez-Alvarez, M.J.; Medina, L.A.; Mora, F.; et al. Small animal PET scanner based on monolithic LYSO crystals: Performance evaluation. *Med. Phys.* **2012**, *39*, 643–653. [[CrossRef](#)] [[PubMed](#)]
69. Yang, Y.; Bec, J.; Zhou, J.; Zhang, M.; Judenhofer, M.S.; Bai, X.; Di, K.; Wu, Y.; Rodriguez, M.; Dokhale, P.; et al. A prototype high-resolution small-animal PET scanner dedicated to mouse brain imaging. *J. Nucl. Med.* **2016**, *57*, 1130–1135. [[CrossRef](#)]
70. Xia, Y.; Ma, T.; Liu, Y.; Wang, S.; Shao, Y. A modified spatial resolution formula for DOI-PET. In Proceedings of the 2011 IEEE Nuclear Science Symposium Conference Record, Valencia, Spain, 23–29 October 2011; pp. 2632–2635.
71. Zhang, X.; Badawi, R.D.; Cherry, S.R.; Qi, J. Theoretical study of the benefit of long axial field-of-view PET on region of interest quantification. *Phys. Med. Biol.* **2018**, *63*, 135010. [[CrossRef](#)]
72. Ito, M.; Lee, J.S.; Kwon, S.I.; Lee, G.S.; Hong, B.; Lee, K.S.; Sim, K.; Lee, S.J.; Rhee, J.T.; Hong, S.J. A four-layer DOI detector with a relative offset for use in an animal PET system. *IEEE Trans. Nucl. Sci.* **2010**, *57*, 976–981. [[CrossRef](#)]
73. Schmall, J.P.; Surti, S.; Karp, J.S. Characterization of stacked-crystal PET detector designs for measurement of both TOF and DOI. *Phys. Med. Biol.* **2015**, *60*, 3549. [[CrossRef](#)]
74. Ren, S.; Yang, Y.; Cherry, S.R. Effects of reflector and crystal surface on the performance of a depth-encoding PET detector with dual-ended readout. *Med. Phys.* **2014**, *41*, 72503. [[CrossRef](#)]
75. Ito, M.; Lee, J.S.; Park, M.J.; Sim, K.S.; Hong, S.J. Design and simulation of a novel method for determining depth-of-interaction in a PET scintillation crystal array using a single-ended readout by a multi-anode PMT. *Phys. Med. Biol.* **2010**, *55*, 3827. [[CrossRef](#)]
76. Zhang, X.; Xie, S.; Yang, J.; Weng, F.; Xu, J.; Huang, Q.; Peng, Q. A depth encoding PET detector using four-crystals-to-one-SiPM coupling and light-sharing window method. *Med. Phys.* **2019**, *46*, 3385–3398. [[CrossRef](#)]
77. Kuang, Z.; Wang, X.; Li, C.; Deng, X.; Feng, K.; Hu, Z.; Fu, X.; Ren, N.; Zhang, X.; Zheng, Y.; et al. Performance of a high-resolution depth encoding PET detector using barium sulfate reflector. *Phys Med Biol.* **2017**, *62*, 5945–5958. [[CrossRef](#)]
78. Schneider, F.R.; Shimazoe, K.; Somlai-Schweiger, I.; Ziegler, S.I. A PET detector prototype based on digital SiPMs and GAGG scintillators. *Phys. Med. Biol.* **2015**, *60*, 1667. [[CrossRef](#)]
79. Lee, S.; Kim, K.Y.; Lee, M.S.; Lee, J.S. Recovery of inter-detector and inter-crystal scattering in brain PET based on LSO and GAGG crystals. *Phys. Med. Biol.* **2020**, *65*, 195005. [[CrossRef](#)]
80. Choghadi, M.A.; Huang, S.C.; Shimazoe, K.; Takahashi, H. Evaluation of dual-ended readout GAGG-based DOI-PET detectors with different surface treatments. *Med. Phys.* **2021**, *48*, 3470–3478. [[CrossRef](#)]
81. Cherry, S.R. The 2006 Henry, N. Wagner Lecture: Of mice and men (and positrons)—advances in PET imaging technology. *J. Nucl. Med.* **2006**, *47*, 1735–1745.
82. Badawi, R.D.; Shi, H.; Hu, P.; Chen, S.; Xu, T.; Price, P.M.; Ding, Y.; Spencer, B.A.; Nardo, L.; Liu, W.; et al. First human imaging studies with the EXPLORER total-body PET scanner. *J. Nucl. Med.* **2019**, *60*, 299–303. [[CrossRef](#)]
83. Poon, J.K.; Dahlbom, M.L.; Moses, W.W.; Balakrishnan, K.; Wang, W.; Cherry, S.R.; Badawi, R.D. Optimal whole-body PET scanner configurations for different volumes of LSO scintillator: A simulation study. *Phys. Med. Biol.* **2012**, *57*, 4077. [[CrossRef](#)]
84. Zhang, X.; Zhou, J.; Cherry, S.R.; Badawi, R.D.; Qi, J. Quantitative image reconstruction for total-body PET imaging using the 2-meter long EXPLORER scanner. *Phys. Med. Biol.* **2017**, *62*, 2465. [[CrossRef](#)]
85. Leung, E.K.; Berg, E.; Omidvari, N.; Spencer, B.A.; Li, E.; Abdelhafez, Y.G.; Schmall, J.P.; Liu, W.; He, L.; Tang, S.; et al. Quantitative accuracy in total-body imaging using the uEXPLORER PET/CT scanner. *Phys. Med. Biol.* **2021**, *66*, 205008. [[CrossRef](#)] [[PubMed](#)]
86. Spencer, B.A.; Berg, E.; Schmall, J.P.; Omidvari, N.; Leung, E.K.; Abdelhafez, Y.G.; Tang, S.; Deng, Z.; Dong, Y.; Lv, Y.; et al. Performance evaluation of the uEXPLORER total-body PET/CT scanner based on NEMA NU 2-2018 with additional tests to characterize PET scanners with a long axial field of view. *J. Nucl. Med.* **2021**, *62*, 861–870. [[CrossRef](#)] [[PubMed](#)]
87. Van Sluis, J.; De Jong, J.; Schaar, J.; Noordzij, W.; Van Snick, P.; Dierckx, R.; Borra, R.; Willemsen, A.; Boellaard, R. Performance characteristics of the digital biograph vision PET/CT system. *J. Nucl. Med.* **2019**, *60*, 1031–1036. [[CrossRef](#)]
88. Prasad, R.; Supanich, M. Performance Characterization of 3D PET System for High Count Dynamic Cardiac Imaging. In Proceedings of the European Congress of Radiology-ECR 2020, Vienna, Austria, 15 January 2020.
89. Pan, T.; Einstein, S.A.; Kappadath, S.C.; Grogg, K.S.; Lois Gomez, C.; Alessio, A.M.; Hunter, W.C.; Fakhri, G.E.; Kinahan, P.E.; Mawlawi, O.R. Performance evaluation of the 5-Ring GE Discovery MI PET/CT system using the national electrical manufacturers association NU 2-2012 Standard. *Med. Phys.* **2019**, *46*, 3025–3033. [[CrossRef](#)] [[PubMed](#)]
90. Chicheportiche, A.; Marciano, R.; Orevi, M. Comparison of NEMA characterizations for Discovery MI and Discovery MI-DR TOF PET/CT systems at different sites and with other commercial PET/CT systems. *EJNMMI Phys.* **2020**, *7*, 1–20. [[CrossRef](#)] [[PubMed](#)]

91. Michopoulou, S.; O'shaughnessy, E.; Thomson, K.; Guy, M.J. Discovery molecular imaging digital ready PET/CT performance evaluation according to the NEMA NU2-2012 standard. *Nucl. Med. Commun.* **2019**, *40*, 270–277. [[CrossRef](#)]
92. Surti, S.; Kuhn, A.; Werner, M.E.; Perkins, A.E.; Kolthammer, J.; Karp, J.S. Performance of Philips Gemini TF PET/CT scanner with special consideration for its time-of-flight imaging capabilities. *J. Nucl. Med.* **2007**, *48*, 471–480.
93. Ingvar, M.; Eriksson, L.; Rogers, G.A.; Stone-Elander, S.; Widen, L. Rapid feasibility studies of tracers for positron emission tomography: High-resolution PET in small animals with kinetic analysis. *J. Cereb. Blood Flow Metab.* **1991**, *11*, 926–931. [[CrossRef](#)] [[PubMed](#)]
94. Chatziioannou, A.F.; Cherry, S.R.; Shao, Y.; Silverman, R.W.; Meadors, K.; Farquhar, T.H.; Pedarsani, M.; Phelps, M.E. Performance evaluation of microPET: A high-resolution lutetium oxyorthosilicate PET scanner for animal imaging. *J. Nucl. Med.* **1999**, *40*, 1164. [[PubMed](#)]
95. Huisman, M.C.; Reeder, S.; Weber, A.W.; Ziegler, S.I.; Schwaiger, M. Performance evaluation of the Philips MOSAIC small animal PET scanner. *Eur. J. Nucl. Med. Mol. Imaging* **2007**, *34*, 532–540. [[CrossRef](#)]
96. Sempere Roldan, P.; Chereul, E.; Dietzel, O.; Magnier, L.; Pautrot, C.; Rbah, L.; Sappey-Mariniere, D.; Wagner, A.; Zimmer, L.; Janier, M.; et al. Raytest ClearPETTM, a new generation small animal PET scanner. *Nucl. Instrum. Methods Phys. Res. A* **2007**, *571*, 498–501. [[CrossRef](#)]
97. Prasad, R.; Ratib, O.; Zaidi, H. Performance evaluation of the FLEX triumph X-PET scanner using the national electrical manufacturers association NU-4 standards. *J. Nucl. Med.* **2010**, *51*, 1608–1615. [[CrossRef](#)] [[PubMed](#)]
98. Wang, L.; Zhu, J.; Liang, X.; Niu, M.; Wu, X.; Kao, C.-M.; Kim, H.; Xie, Q. Performance evaluation of the Trans-PET[®] BioCalibur[®] LH system: A large FOV small-animal PET system. *Phys. Med. Biol.* **2014**, *60*, 137–150. [[CrossRef](#)] [[PubMed](#)]
99. Miwa, K.; Inubushi, M.; Takeuchi, Y.; Katafuchi, T.; Koizumi, M.; Saga, T.; Sasaki, M. Performance characteristics of a novel clustered multi-pinhole technology for simultaneous high-resolution SPECT/PET. *Ann. Nucl. Med.* **2015**, *29*, 460–466. [[CrossRef](#)]
100. Krishnamoorthy, S.; Blankemeyer, E.; Mollet, P.; Surti, S.; Holen, R.V.; Karp, J.S. Performance evaluation of the MOLECUBES β -CUBE—a high spatial resolution and high sensitivity small animal PET scanner utilizing monolithic LYSO scintillation detectors. *Phys. Med. Biol.* **2018**, *63*, 155013. [[CrossRef](#)]
101. Keller, S.H.; Svarer, C.; Sibomana, M. Attenuation correction for the HRRT PET-scanner using transmission scatter correction and total variation regularization. *IEEE Trans. Med. Imaging* **2013**, *32*, 1611–1621. [[CrossRef](#)]
102. De Jong, H.W.; Van Velden, F.H.; Kloet, R.W.; Buijs, F.L.; Boellaard, R.; Lammertsma, A.A. Performance evaluation of the ECAT HRRT: An LSO-LYSO double layer high resolution, high sensitivity scanner. *Phys. Med. Biol.* **2007**, *52*, 1505. [[CrossRef](#)] [[PubMed](#)]
103. De Jong, H.W.; Boellaard, R.; Knoess, C.; Lenox, M.; Michel, C.; Casey, M.; Lammertsma, A.A. Correction methods for missing data in sinograms of the HRRT PET scanner. *IEEE Trans. Nucl. Sci.* **2003**, *50*, 1452–1456. [[CrossRef](#)]
104. Dubois, B.; Feldman, H.H.; Jacova, C.; Dekosky, S.T.; Barberger-Gateau, P.; Cummings, J.; Delocourte, A.; Galasko, D.; Gauthier, S.; Jicha, G.; et al. Research criteria for the diagnosis of Alzheimer's disease: Revising the NINCDS-ADRDA criteria. *Lancet Neurol.* **2007**, *6*, 734–746. [[CrossRef](#)]
105. Emsen, B.; Villafane, G.; David, J.P.; Evangelista, E.; Chalaye, J.; Lerman, L.; Authier, F.J.; Gracies, J.M.; Itti, E. Clinical impact of dual-tracer FDOPA and FDG PET/CT for the evaluation of patients with parkinsonian syndromes. *Medicine* **2020**, *99*, e23060. [[CrossRef](#)]
106. Tian, M.; Watanabe, Y.; Kang, K.W.; Murakami, K.; Chiti, A.; Carrio, I.; Civelek, A.C.; Feng, J.; Zhu, Y.; Zhou, R. International consensus on the use of [18F]-FDG PET/CT in pediatric patients affected by epilepsy. *Eur. J. Nucl. Med. Mol. Imaging* **2021**, *48*, 3827–3834. [[CrossRef](#)] [[PubMed](#)]
107. Yamamoto, S.; Honda, M.; Oohashi, T.; Shimizu, K.; Senda, M. Development of a brain PET system, PET-Hat: A wearable PET system for brain research. *IEEE Trans. Nucl. Sci.* **2011**, *58*, 668–673. [[CrossRef](#)]
108. Melroy, S.; Bauer, C.; McHugh, M.; Carden, G.; Stolin, A.; Majewski, S.; Breczynski-Lewis, J.; Wuest, T. Development and design of next-generation head-mounted ambulatory microdose positron-emission tomography (AM-PET) system. *Sensors* **2017**, *17*, 1164. [[CrossRef](#)] [[PubMed](#)]
109. Hernandez, T.G.; Gonzalez, A.V.; Rebolledo, J.F.; Jurado, R.S.; Ferrando, J.R.; Gonzalez, L.B.; Cabanero, D.G.; Santiago, M.D.C. Performance evaluation of a high resolution dedicated breast PET scanner. *Med. Phys.* **2016**, *43*, 2261–2272. [[CrossRef](#)]
110. Rosen, E.L.; Turkington, T.G.; Soo, M.S.; Baker, J.A.; Coleman, R.E. Detection of primary breast carcinoma with a dedicated, large-field-of-view FDG PET mammography device: Initial experience. *Radiology* **2005**, *234*, 527–534. [[CrossRef](#)]
111. Bowen, S.L.; Wu, Y.; Chaudhari, A.J.; Fu, L.; Packard, N.J.; Burkett, G.W.; Yang, K.; Lindfors, K.K.; Shelton, D.K.; Hagge, R.; et al. Initial characterization of a dedicated breast PET/CT scanner during human imaging. *J. Nucl. Med.* **2009**, *50*, 1401–1408. [[CrossRef](#)] [[PubMed](#)]
112. Raylman, R.R.; Majewski, S.; Smith, M.F.; Proffitt, J.; Hammond, W.; Srinivasan, A.; McKisson, J.; Popov, V.; Weisenberger, A.; Judy, C.O.; et al. The positron emission mammography/tomography breast imaging and biopsy system (PEM/PET): Design, construction and phantom-based measurements. *Phys. Med. Biol.* **2008**, *53*, 637. [[CrossRef](#)] [[PubMed](#)]